

# Three-dimensional collective charge excitations in electron-doped copper oxide superconductors

M. Hepting<sup>1</sup>, L. Chaix<sup>1,9</sup>, E. W. Huang<sup>1,2</sup>, R. Fumagalli<sup>3</sup>, Y. Y. Peng<sup>3,10</sup>, B. Moritz<sup>1</sup>, K. Kummer<sup>4</sup>, N. B. Brookes<sup>4</sup>, W. C. Lee<sup>5</sup>, M. Hashimoto<sup>6</sup>, T. Sarkar<sup>7</sup>, J.-F. He<sup>1,11</sup>, C. R. Rotundu<sup>1</sup>, Y. S. Lee<sup>1</sup>, R. L. Greene<sup>7</sup>, L. Braicovich<sup>3,4</sup>, G. Ghiringhelli<sup>3,8</sup>, Z. X. Shen<sup>1\*</sup>, T. P. Devereaux<sup>1\*</sup> & W. S. Lee<sup>1\*</sup>

High-temperature copper oxide superconductors consist of stacked CuO2 planes, with electronic band structures and magnetic excitations that are primarily two-dimensional<sup>1,2</sup>, but with superconducting coherence that is three-dimensional. This dichotomy highlights the importance of out-of-plane charge dynamics, which has been found to be incoherent in the normal state<sup>3,4</sup> within the limited range of momenta accessible by optics. Here we use resonant inelastic X-ray scattering to explore the charge dynamics across all three dimensions of the Brillouin zone. Polarization analysis of recently discovered collective excitations (modes) in electron-doped copper oxides<sup>5-7</sup> reveals their charge origin, that is, without mixing with magnetic components<sup>5-</sup> The excitations disperse along both the in-plane and out-of-plane directions, revealing its three-dimensional nature. The periodicity of the out-of-plane dispersion corresponds to the distance between neighbouring CuO<sub>2</sub> planes rather than to the crystallographic c-axis lattice constant, suggesting that the interplane Coulomb interaction is responsible for the coherent out-of-plane charge dynamics. The observed properties are hallmarks of the long-sought 'acoustic plasmon', which is a branch of distinct charge collective modes predicted for layered systems<sup>8-12</sup> and argued to play a substantial part in mediating high-temperature superconductivity<sup>10-12</sup>.

The charge dynamics of systems with periodically stacked quasi-two-dimensional (2D) conducting planes are strongly affected in the presence of poorly screened interplane Coulomb interactions. In a simple layered electron gas with conducting planes separated by dielectric spacers<sup>8,9</sup>, the dispersion of plasmons (that is, the collective dynamical charge modes) changes from optical-like to acoustic-like as a function of out-of-plane momenta  $q_z$  (Fig. 1a) (such plasmons are referred to as 'acoustic plasmons' hereafter), a behaviour distinct from that in either pure 2D or isotropic 3D systems. For superconducting copper oxides, similar charge dynamics have been postulated because they consist of conducting CuO<sub>2</sub> planes stacked along the c-axis with poor out-of-plane Coulomb screening<sup>10–12</sup>. Although plasmons have been observed in various spectroscopic studies at the Brillouin zone centre<sup>4,13,14</sup> and also by transmission electron energy loss spectroscopy (EELS), which typically explores in-plane energy-momenta dispersions at  $q_z = 0$  (ref. <sup>15</sup>), there is no information on its possible  $q_z$  dependence. Experimental evidence of this previously undetected component and its characterization in energy and momentum can shed new light on long-standing hypotheses that connect out-of-plane charge dynamics to superconductivity. For instance, it has been proposed that 20% of the observed value of the high superconducting transition temperature  $T_c$  of the copper oxides can be attributed to the presence of acoustic plasmons<sup>10–12</sup>, where the large amount of energy stored in the interplane Coulomb interactions is related to the

substantial energy savings associated with the high superconducting transition temperature  $^{16,17}$ .

In this Letter, we focus our attention on the enigmatic 'zone centre' excitation previously discovered by Cu L-edge resonant inelastic X-ray scattering (RIXS) in the electron-doped copper oxide  $\mathrm{Nd}_{2-x}\mathrm{Ce}_x\mathrm{CuO}_4$  (NCCO)  $(x=0.15)^{5.6}$  and  $\mathrm{Sr}_{1-x}\mathrm{La}_x\mathrm{CuO}_2$  (ref. <sup>7</sup>). In a different family of electron-doped copper oxides  $\mathrm{La}_{2-x}\mathrm{Ce}_x\mathrm{CuO}_4$  (LCCO) (x=0.175), we resolve spectral features that are similar to those of NCCO at representative in-plane momentum transfers  $q_{\parallel}$  (red-shaded peak in Fig. 1b, c), suggesting the universality of this collective mode in electron-doped copper oxides. Speculation about its origin has included intra-band transitions<sup>5</sup>, collective modes of a quantum phase<sup>6</sup>, and plasmons<sup>18</sup>. Although the mode has been suspected to be of charge character, a definitive assessment has not been possible owing to the inability to distinguish between charge and magnetic excitations in previous measurements<sup>19,20</sup>.

We first identify the character of this excitation by determining the associated magnetic and charge contributions to the RIXS spectra. This can be uniquely achieved by resolving the polarization of both the incident and scattered photons<sup>19</sup>. Namely, magnetic excitations flip spins and necessarily change the angular momentum of the photons in the scattering process, that is, contribute to the crossed-polarization channel ( $\sigma\pi$  or  $\pi\sigma$ ). Conversely, charge excitations preserve the angular momentum of the photon and contribute to the parallel polarization channel ( $\sigma\sigma$  or  $\pi\pi$ ). Figure 1d, e shows polarization-resolved RIXS spectra for two different in-plane momenta. At  $q_{\parallel} = (0.045, 0)$  the features of the zone centre excitation are fully suppressed for crossed polarizations ( $\sigma\pi$ ) and the spectrum contains only the parallel polarization ( $\sigma\sigma$ ) contribution. For larger momentum transfer  $q_{\parallel} = (0.095,$ 0) the mode disperses towards higher energy (about 0.8 eV) (Fig. 1e) and the well-studied paramagnon excitation<sup>5–7,20</sup> emerges on a lower energy scale (about 0.3 eV). As expected, the paramagnon yields spectral weight in both polarizations owing to the mixture of single spin-flip excitation, double spin-flip and incoherent particle-hole charge excitations, whose spectral weight increases with increasing doping concentration<sup>21</sup>. Importantly, the zone centre excitations, which are separated in energy from the paramagnons, still appear only for parallel polarization geometries. Thus, we first conclude that the zone centre excitations are a branch of pure charge modes.

A second insight can be obtained from a comprehensive mapping of the energy–momentum dispersion in all three dimensions of reciprocal space, in contrast to previous RIXS experiments that explored the projected in-plane momentum without focusing on the  $q_z$  dependence<sup>6–8</sup>. Figure 2a, b shows the RIXS intensity maps as a function of momentum transfer along the hh- and h-directions (that is, along (0, 0, l)–(h, h, l) and (0, 0, l)–(h, 0, l), respectively) at l = 1 and l = 1.65. We denote

<sup>1</sup>Stanford Institute for Materials and Energy Sciences, SLAC National Accelerator Laboratory and Stanford University, Menlo Park, CA, USA. <sup>2</sup>Department of Physics, Stanford University, Stanford, CA, USA. <sup>3</sup>Dipartimento di Fisica, Politecnico di Milano, Milan, Italy. <sup>4</sup>European Synchrotron Radiation Facility (ESRF), Grenoble, France. <sup>5</sup>Department of Physics, Binghamton University, Binghamton, NY, USA. <sup>6</sup>Stanford Synchrotron Radiation Lightsource, SLAC National Accelerator Laboratory, Menlo Park, CA, USA. <sup>7</sup>Department of Physics, Center for Nanophysics and Advanced Materials, University of Maryland, College Park, MD, USA. <sup>8</sup>CNR-SPIN, Politecnico di Milano, Milan, Italy. <sup>9</sup>Present address: Université Grenoble Alpes, CNRS, Institut Néel, Grenoble, France. <sup>10</sup>Present address: Department of Physics and Seitz Materials Research Lab, University of Illinois, Urbana, IL, USA. <sup>11</sup>Present address: Department of Physics, University of Science and Technology of China, Hefei, China. \*e-mail: zyshen@stanford.edu; tpd@stanford.edu; leews@stanford.edu

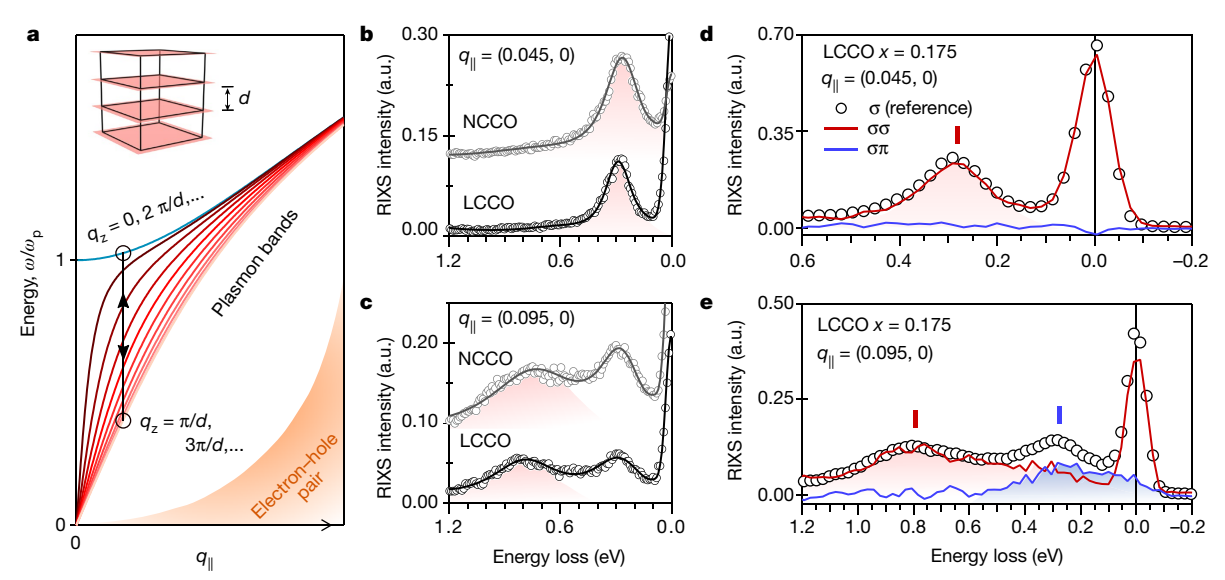


Fig. 1 | Plasmons in a layered electron gas and dispersive charge excitations in electron-doped copper oxides. a, Plasmon dispersion in a layered electron gas as a function of in- and out-of-plane momentum transfer  $q_{\parallel}$  and  $q_z$ , respectively. Different branches correspond to specific out-of-plane momentum transfers  $q_z$  and are a result of the interplane Coulomb interaction between the periodically stacked planes with distance d (see inset). Their spectrum varies from a single optical branch (light blue line) with the characteristic plasma frequency  $\omega_p$  for  $q_z = 0$ ,  $2\pi/d$ ,... to a range of acoustic branches (light red lines) with the lowest-energy branch for  $q_z = \pi/d$ ,  $3\pi/d$ . The electron-hole pair excitation continuum is illustrated by the orange shaded area. b, c, RIXS spectra of NCCO (x = 0.15) and LCCO (x = 0.175) at in-plane momentum transfers  $q_{\parallel} = (0.045, 0)$  and (0.095, 0) for incident photon energies tuned

to the Cu L<sub>3</sub>-edge at temperature  $T \approx 20$  K. The spectral peak assigned to the dispersive zone centre excitation is highlighted by the red-shaded peak profile. The additional peak at about 0.3 eV in **c** is identified as the paramagnon, justified by the polarization-resolved RIXS spectra shown in **e**. The NCCO and LCCO spectra are offset in the vertical direction for clarity. **d**, **e**, Polarization-resolved RIXS spectra of LCCO at  $q_{\parallel} = (0.045, 0)$  and (0.095, 0). Charge excitations are detected in the parallel polarization channel  $(\sigma\sigma, \text{red line})$  while magnetic excitations are detected in the spin-flip crossed-polarization channel  $(\sigma\pi, \text{blue line})$ . The reference spectrum (open symbols) is taken with  $\sigma$  polarized incident photons in the absence of polarization analysis, corresponding thus to the sum of  $\sigma\sigma$  and  $\sigma\pi$ . Red and blue markers indicate the relevant spectral weight maximum of the  $\sigma\sigma$  and  $\sigma\pi$  channel, respectively. a.u., arbitrary units.

momentum transfer h, k, l in reciprocal lattice units  $(2\pi/a, 2\pi/b, 2\pi/c)$ , where a, b = 4.01 Å and c = 12.4 Å are the lattice constants of LCCO with x = 0.175. For both l, the excitations exhibit an almost linear dispersion emanating away from (0,0,l) along both the hh- and h directions. Surprisingly, while the paramagnons do not disperse appreciably with different l values (as expected for the quasi-2D magnetic structure of copper oxides), the dispersion of the zone centre excitation becomes steeper and increasingly separated from the paramagnon branch at larger l. This behaviour is highlighted in Fig. 2c. The raw data itself also clearly shows such an l-dependence: the spectral peak shifts to higher energy and becomes broader at the higher l-value for a given in-plane momentum (Fig. 2d, e, Extended Data Figs. 1, 2).

To further investigate the out-of-plane dependence, Fig. 3a displays the energy–momentum dispersion as a function of l at fixed in-plane momentum transfer (0.025,0) near the in-plane zone centre. As anticipated, the dispersion is symmetric around the out-of-plane zone centre l=1 as it is a high symmetry point in reciprocal space. Remarkably, the zone centre excitation continues dispersing towards high energy with further increasing l, insensitive to the next high symmetry point at l=1.5. In fact, the energy scale of the excitation continues to increase even at l=1.8, the highest out-of-plane momentum transfer that was accessible in our experiment. We also observe the same peculiar behaviour in our momentum-resolved RIXS measurements on NCCO (see Extended Data Fig. 3), suggesting a universal origin of the branch of charge modes from the three-dimensional (3D) nature of the Coulomb interaction in an otherwise layered quasi-2D material.

These results can be rationalized by doubling the out-of-plane Brillouin zone size, implying that the crystallographic unit cell with lattice constant c does not set the periodicity of the zone centre excitation, but rather d=c/2: the nearest-neighbour  ${\rm CuO_2}$  plane spacing (Fig. 3b). Hence, a new index  $l^*$  in units of  $2\pi/d$  appropriately describes the Brillouin zone that is 'felt' by the zone centre excitation and establishes the proper periodicity of the dispersion. An obvious mechanism

that could induce such a Brillouin zone 'reconstruction' in a quasi-2D system is the interplanar Coulomb interaction.

These striking features are reminiscent of acoustic plasmon bands theoretically proposed in the aforementioned layered electron gas model (Fig. 1a), which provides a qualitative fit to the observed zone centre excitation (see Methods and Extended Data Fig. 4 for the fits). To demonstrate the behaviour of collective charge dynamics beyond this weakly correlated layered electron gas model, we perform determinant quantum Monte Carlo (DQMC) calculations for a 2D three-band Hubbard model with an electron doping of x = 0.18 and incorporate three-dimensionality through interplane Coulomb interactions using a random-phase-approximation-like formalism (see Methods). Therewith, we obtain the collective charge response via the loss function  $-\text{Im}(1/\varepsilon)$ , where  $\varepsilon$  is the dielectric function, versus the out-of-plane momentum transfer  $l^*$ . As shown in Fig. 3c, the calculated dispersions along the  $l^*$ -direction at the in-plane momenta accessible in our  $16 \times 4$  cluster exhibit the same qualitative behaviours observed in both LCCO (Fig. 3a) and NCCO (Extended Data Fig. 3). We note that recent calculations using different methods and models have also demonstrated l\*-dependent plasmon bands 18,22. Although RIXS is not simply proportional to  $-\text{Im}(1/\varepsilon)$  owing to the resonant process<sup>19,23</sup> it nevertheless can contain critical information on the loss function, such as the dispersion of excitations. Thus, the agreement between our data and theory lends strong support to the idea of attributing the zone centre mode to plasmon excitations, with momentum-resolved RIXS providing access to its acoustic bands.

Interestingly, the data shown in Figs. 2, 3a indicate that the plasmon peak broadens when approaching the equivalent zone centre  $(0,0,l^*=1)$  along the  $l^*$ -direction (see also Extended Data Figs. 1c, 3c). In fact, at momentum transfer  $(0.025,0,l^*=0.925)$ , that is, close to the equivalent zone centre  $(0,0,l^*=1)$ , the plasmon linewidth of approximately 0.5 eV (Fig. 3a) is similar to previous transmission EELS reports  $l^5$  and optical conductivity measurements at  $(0,0,0)^{14}$ . The increasing incoherence of the mode near the zone centre is consistent

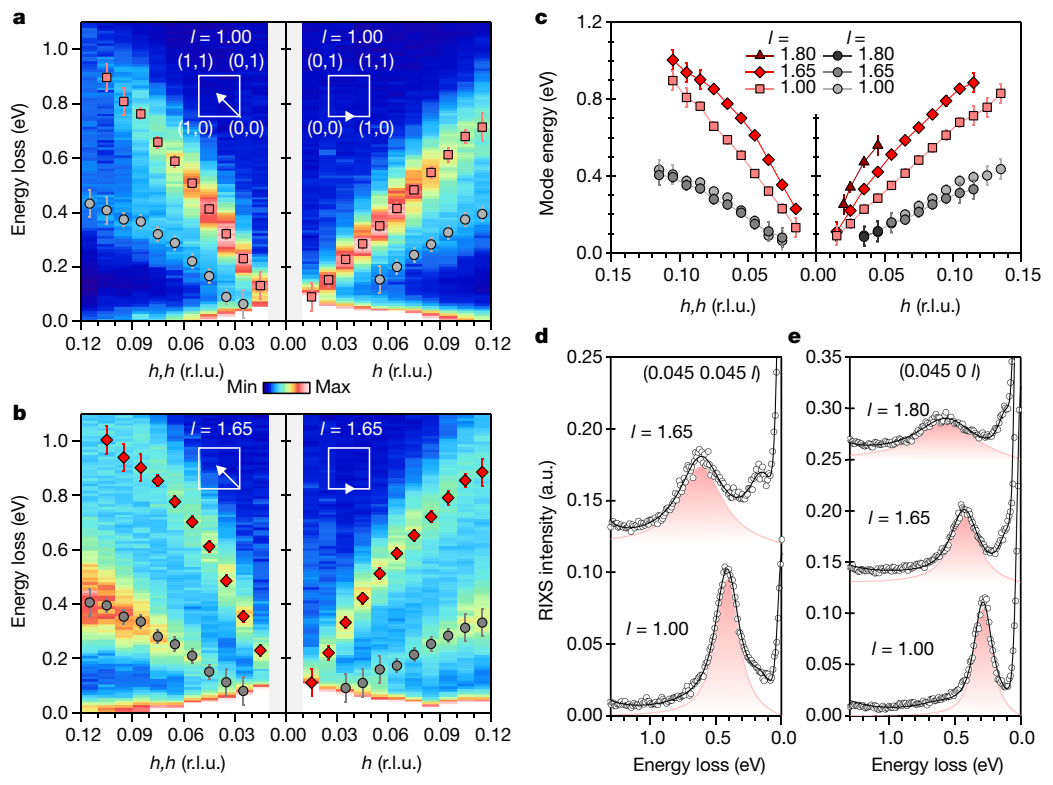


**Fig. 2** | Three-dimensionality of the zone centre excitations. **a**, **b**, RIXS intensity maps of LCCO (x=0.175) for momentum transfer along the hh- and h- directions at l=1 and l=1.65. Red and grey symbols indicate least-squares-fit peak positions of the zone centre excitation and the paramagnon, respectively (see Extended Data Figs. 1 and 2). Error bars are estimated from the uncertainty in energy-loss reference-point determination ( $\pm 0.01$  eV) together with the standard deviation of the fits. The insets indicate the probe direction in reciprocal space. **c**, Summary of the energy dispersion of the zone centre excitation (red symbols) and the paramagnon

(grey symbols) for different l-values, that is, for different momentum transfers along the c-axis. The energy dispersion of the paramagnon is independent of l within the experimental error. The lines connecting markers serve as a guide for the eye.  $\mathbf{d}$ ,  $\mathbf{e}$ , Representative raw RIXS spectra (open symbols) for momentum transfer along the hh- and h- directions at different l-values, together with the anti-symmetrized Lorentzian fit profiles of the zone centre excitation (red shades) and the sum of all contributions fitted to the spectra (solid black lines, see also Extended Data Figs. 1 and 2). Spectra are offset in the vertical direction for clarity. r.l.u., reciprocal lattice unit.

with incoherent charge dynamics inferred from *c*-axis optical conductivity<sup>3,4</sup>. However, such linewidth evolution appears to be different from the Landau quasi-particle picture in which the plasmon peak should be sharpest at the zone centre where the particle–hole (Landau) continuum is minimal and well separated from the plasmon. Other mechanisms, such as the presence of non-Fermi-liquid-producing interactions, polar interlayer electron–phonon coupling<sup>24</sup> and Umklapp scattering<sup>25</sup>, may reconcile these observations.

We now investigate the acoustic plasmon bands in LCCO as a function of the carrier density, which is nominally the Ce concentration x. We have also verified the systematics of doping concentration among different samples using an internal spectral reference—the dd excitations of RIXS spectra (Methods and Extended Data Fig. 5). As shown in Fig. 4a, b, the plasmon bands exhibit a detectable doping dependence. In a naive picture of the free electron model, the plasmon energy is expected to increase proportionally to  $\sqrt{x/m^*}$ , where  $m^*$  is the effective electron mass. Consistent with such an expectation the mode energies of x = 0.11 to about 0.15 increase linearly with  $\sqrt{x}$  (Fig. 4c), further substantiating the attribution of the zone centre excitation to a plasmon. However, for higher dopings, the rate of increase slows down and appears to hit a plateau for x = 0.17 and 0.18. This observation suggests a possible variation in the band dispersion or Fermi surface at approximately  $x \approx 0.15$ . Recent Hall-effect measurements on LCCO have indicated Fermi-surface reconstruction due to antiferromagnetic correlations ending at around  $x \approx 0.14$  (ref. <sup>26</sup>), corroborating our observation.

We note that our observation appears to be distinct from a recent high-resolution EELS measurement, which reported featureless in-plane charge excitations in a hole-doped copper oxide<sup>27</sup>. This

suggests a distinct behaviour of the charge degrees of freedom between electron- and hole-doped copper oxides. However, given the similarities of the layered 2D  $\rm CuO_2$  plane structure between electron- and hole-doped materials, we should expect a similar three-dimensionality in the charge dynamics of the hole-doped copper oxides. Although previous RIXS studies on hole-doped compounds primarily focused on magnetic, orbital and other high-energy excitations<sup>20</sup>, few investigated the region of energy–momentum space necessary to identify and characterize the acoustic plasmon<sup>28</sup>. More detailed RIXS measurements on hole-doped compounds, in both single and multi-layer systems with higher  $T_{\rm C}$ , will be able to clarify these issues.

Our observation of 3D plasmon modes indicates that the copper oxides, at the very least, should be modelled as layered 2D systems when describing their charge dynamics, a fact that is often overlooked. This change of perspective has important implications. First, in a 2D doped Mott insulator, the in-plane charge fluctuations are strongly suppressed by the Coulomb interaction. Thus the spin dynamics become the most prominent low-energy excitations, thought to be most relevant to high- $T_{\rm c}$  superconductivity<sup>29</sup>. Our results challenge this view by demonstrating that the low energy charge fluctuations can be quite active owing to the layered structure of the copper oxide. Early theories suggested that acoustic plasmons may be able to mediate pairing<sup>10</sup>, or perhaps more importantly, enhance  $T_c$  for Cooper pairs bound by other interactions<sup>12</sup>. Second, the Coulomb energy stored between CuO<sub>2</sub> planes can be important and may play a part in the energy savings associated with the superconducting transition 16,17. Third, the energy of the plasmon extrapolates to approximately zero at the projected zone centre. This implies a negligible single electron hopping between adjacent CuO<sub>2</sub> planes, leaving the Coulomb interaction as the sole

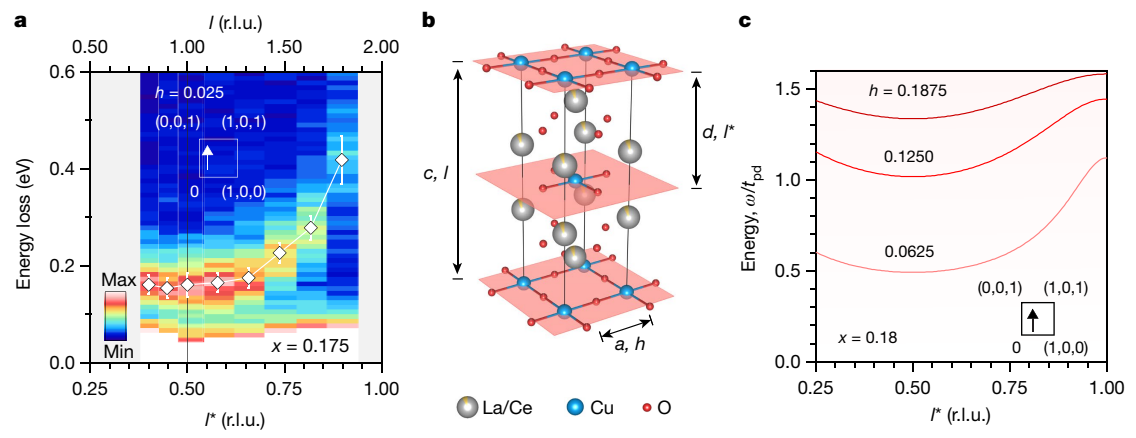


**Fig. 3** | **Out-of-plane plasmon dispersion.** a, RIXS intensity map of LCCO (x=0.175) for momentum transfer along the out-of-plane direction at h=0.025. The out-of-plane momentum is indicated by the indices l (top scale, units of  $2\pi/c$ ) corresponding to the crystallographic c-axis, and  $l^*$  (bottom scale, units of  $2\pi/d$ ) corresponding to the CuO<sub>2</sub> plane spacing. White symbols indicate fitted peak positions of the zone centre excitation. The black vertical line highlights the high symmetry point at  $l^*=0.5$  (that is, l=1.0). Error bars are estimated from the uncertainty in energy-loss reference-point determination ( $\pm 0.01$  eV)

together with the standard deviation of the fits. **b**, Crystal structure of LCCO with the crystallographic unit cell indicated by black lines and the CuO<sub>2</sub> planes in red. **c**, Calculation of the charge dynamics for planes of a stacked three-band Hubbard model (see Methods) with electron doping x = 0.18. The peak frequency of the loss function  $-\text{Im}(1/\varepsilon)$  is plotted versus the out-of-plane momentum transfer  $l^*$  at h = 0.1875, 0.1250 and 0.0625. The energy is expressed in units of  $t_{\rm pd}$ , the hopping integral between the oxygen 2p and Cu 3d orbitals in the three-band Hubbard model.

source of interplanar coupling. Such restriction of the charge to the 2D planes may enhance the effects of quantum confinement at the heart of topological theories for superconductivity in copper oxides<sup>30,31</sup>. However, important questions remain about the impact of the interplanar Coulomb interaction on the electronic structure, the pseudogap and charge- and spin-density-wave orders. In a broader context, our result fits within the general framework that the Coulomb interaction

affects charge dynamics in nanoscale heterostructures of 2D quantum materials, including transitional metal chalcogenides and graphene. Manipulating the Coulomb interaction could enable fine-tuning of desired properties of artificial quantum materials, such as plasmonics in nanostructures, with a range of applications from sensors to photonic and electronic devices for communications (for example, see the Plasmonics Focus Issue introduced in ref. <sup>32</sup>).

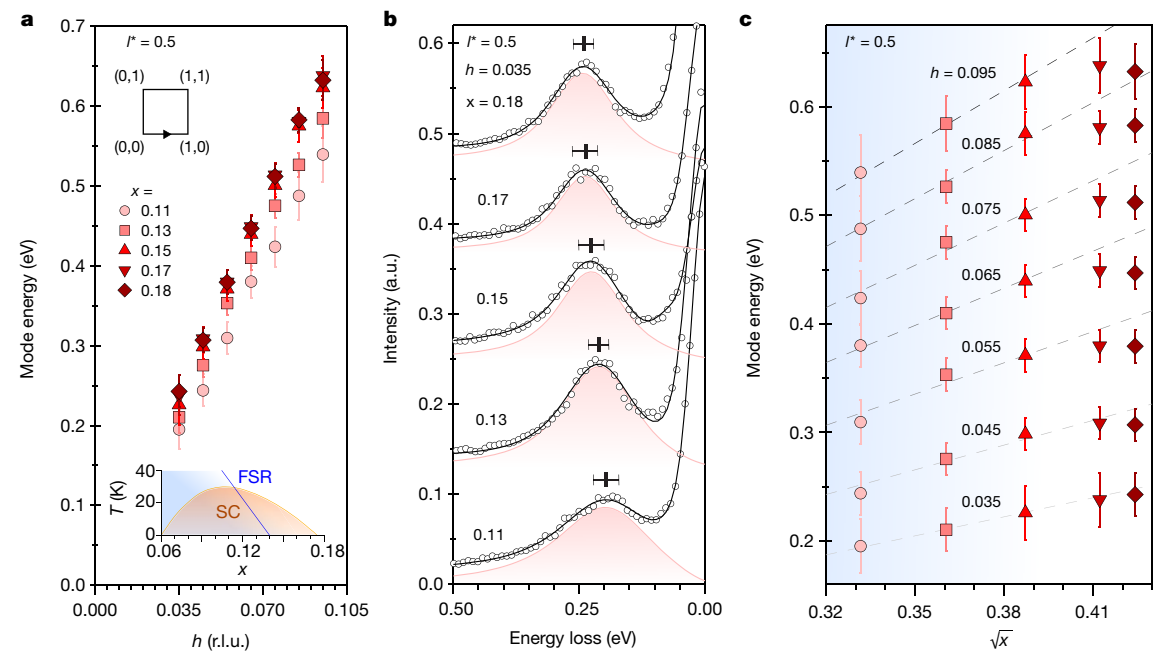


**Fig. 4** | **Doping dependence of the plasmon. a**, Energy dispersion of the LCCO zone centre mode for momentum transfer along the h-direction at  $l^* = 0.5$ . Red symbols are the fitted peak positions for Ce doping concentrations x = 0.11, 0.13, 0.15, 0.17 and 0.18. The bottom inset shows the temperature versus doping phase diagram of LCCO thin films adapted from ref. <sup>29</sup> including a superconducting dome (orange shading, SC) and a small Fermi surface region (blue shading) undergoing a crossover to a reconstructed Fermi surface (blue line, FSR) that ends at  $x \approx 0.14$ . **b**, Representative raw RIXS spectra (open symbols) for momentum transfer h = 0.035 and  $l^* = 0.5$  for different dopings. The anti-symmetrized Lorentzian fit profiles are shaded in red with vertical black markers

indicating the peak positions and the horizontal bars indicating the error bars. Spectra are offset in the vertical direction for clarity. **c**, Mode energies versus the square root of x for in-plane momenta from h=0.035 to h=0.095 at  $l^*=0.5$ . The symbol style refers to the dopings as indicated in **a**. Dashed lines are linear fits of the mode energy versus  $\sqrt{x}$  for dopings x=0.11 to 0.15, constrained by assuming that the mode energy is 0 at x=0. We note that the rate of increase deviates from linear behaviour and forms a plateau for higher doping, as mentioned in the text. Error bars in this figure are estimated from the uncertainty in energy-loss reference-point determination ( $\pm 0.01$  eV) together with the standard deviation of the fits.



## Online content

Any methods, additional references, Nature Research reporting summaries, source data, statements of data availability and associated accession codes are available at https://doi.org/10.1038/s41586-018-0648-3.

Received: 2 May 2018; Accepted: 22 August 2018; Published online 31 October 2018.

- Damascelli, A., Hussain, Z. & Shen, Z. X. Angle-resolved photoemission studies of the cuprate superconductors. Rev. Mod. Phys. 75, 473 (2003).
- Fujita, M. et al. Progress in neutron scattering studies of spin excitations in high-T<sub>c</sub> cuprates. J. Phys. Soc. Jpn. 81, 011007 (2012).
- Tajima, S. Optical studies of high-temperature superconducting cuprates. Rep. Prog. Phys. 79, 094001 (2016).
- Singley, E. J., Basov, D. N., Kurahashi, K., Uefuji, T. & Yamada, K. Electron dynamics in Nd<sub>1.85</sub>Ce<sub>0.15</sub>CuO<sub>4+6</sub>: evidence for the pseudogap state and unconventional c-axis response. *Phys. Rev. B* 64, 224503 (2001).
- Ishii, K. et al. High-energy spin and charge excitations in electron-doped copper oxide superconductors. Nat. Commun. 5, 3714 (2014).
- Lee, W. S. et al. Asymmetry of collective excitations in electron- and hole-doped cuprate superconductors. Nat. Phys. 10, 883 (2014).
- Dellea, G. et al. Spin and charge excitations in artificial artificial hole- and electron-doped infinite layer cuprate superconductors. *Phys. Rev. B* 96, 115117 (2017).
- Grecu, D. Plasmon frequency of the electron gas in layered structures. *Phys. Rev. B* 8, 1958 (1973).
- Fetter, A. L. Electrodynamics of a layered electron gas II. Periodic array. Ann. Phys. 88, 1 (1974).
- Kresin, V. Z. & Morawitz, H. Layer plasmons and high-T<sub>c</sub> superconductivity. Phys. Rev. B 37, 7854 (1988).
- Ishii, Y. & Ruvalds, J. Acoustic plasmons and cuprate superconductivity. Phys. Rev. B 48, 3455 (1993).
- Bill, A., Morawitz, H. & Kresin, V. Z. Electronic collective modes and superconductivity in layered conductors. *Phys. Rev. B* 68, 144519 (2003).
- 13. Bozovic, I. Plasmons in cuprate superconductors. Phys. Rev. B 42, 1969 (1990).
- Levallois, J. et al. Temperature-dependent ellipsometry measurements of partial coulomb energy in superconducting cuprates. *Phys. Rev. X* 6, 031027 (2016).
- Fink, J., Knupfer, M., Atzkern, S. & Golden, M. Electronic correlation in solids, studies using electron energy-loss spectroscopy. J. Elec. Spectrosc. Rel. Phenom. 117/118, 287–309 (2001).
- Leggett, A. J. Where is the energy saved in cuprate superconductivity? J. Phys. Chem. Solids 59, 1729 (1998).
- Leggett, A. J. Cuprate superconductivity: dependence of T<sub>c</sub> on the c-axis layering structure. Phys. Rev. Lett. 83, 392 (1999).
- Greco, A., Yamase, H. & Bejas, M. Plasmon excitations in layered high-T<sub>c</sub> cuprates. Phys. Rev. B 94, 075139 (2016).
- Jia, C., Wohlfeld, K., Wang, Y., Moritz, B. & Devereaux, T. P. Using RIXS to uncover elementary charge and spin excitations. *Phys. Rev. X* 6, 021020 (2016).
  Ament, L. J. P., van Veenendaal, M., Devereaux, T. P., Hill, J. P. & van den Brink, J.
- Ament, L. J. P., van Veenendaal, M., Devereaux, T. P., Hill, J. P. & van den Brink, J. Resonant inelastic X-ray scattering studies of elementary excitations. Rev. Mod. Phys. 83, 705 (2011).
- Huang, H. Y. et al. Raman and fluorescence characteristics of resonant inelastic X-ray scattering from doped superconducting cuprates. Sci. Rep. 6, 19657 (2016).
- Markiewicz, R. S., Hasan, M. Z. & Bansil, A. Acoustic plasmons and doping evolution of Mott physics in resonant inelastic X-ray scattering from cuprate superconductors. *Phys. Rev. B* 77, 094518 (2008).
- Kim, J. et al. Comparison of resonant inelastic X-ray scattering spectra and dielectric loss functions in copper oxides. *Phys. Rev. B* 79, 094525 (2009).

- Meevasana, W., Devereaux, T. P., Nagaosa, N., Shen, Z. X. & Zaanen, J. Calculation of overdamped c-axis charge dynamics and the coupling to polar phonons in cuprate superconductors. *Phys. Rev. B* 74, 174524 (2006).
- Lee, W. C. Superconductivity-induced changes in density-density correlation function enabled by Umklapp processes. Phys. Rev. B 91, 224503 (2015).
- Sarkar, T. et al. Fermi surface reconstruction and anomalous low-temperature resistivity in electron-doped La<sub>1-x</sub>Ce<sub>x</sub>CuO<sub>4</sub>. Phys. Rev. B 96, 155449 (2017).
- Mitrano, M. et al. Anomalous density fluctuation in a strange metal. Proc. Natl Acad. Sci. USA 115, 5392 (2018).
- Ishii, K. et al. Observation of momentum-dependent charge excitations in hole-doped cuprates using resonant inelastic X-ray scattering at the oxygen K edge. Phys. Rev. B 96, 115148 (2017).
- Scalapino, D. J. et al. A common thread: the pairing interaction for unconventional superconductors. Rev. Mod. Phys. 84, 1383 (2012)
- Clarke, D. G., Strong, S. P. & Anderson, P. W. Incoherence of single particle hopping between Luttinger liquids. *Phys. Rev. Lett.* 72, 3218 (1994).
- Sachdev, S. & Chowdhury, D. The novel metallic states of the cuprates: Fermi liquids with topological order, and strange metals. *Prog. Theor. Exp. Phys.* 2016, 12C102 (2016).
- 32. Pile, D. Perspective on plasmonics. Nat. Photon. 6, 714-715 (2012).

Acknowledgements This work is supported by the US Department of Energy (DOE), Office of Science, Basic Energy Sciences, Materials Sciences and Engineering Division, under contract DE-ACO2-76SF00515. L.C. acknowledges support from the Department of Energy, SLAC Laboratory Directed Research and Development funder contract under DE-ACO2-76SF00515. RIXS data were taken at beamline ID32 of the European Synchrotron Radiation Facility (ESRF, Grenoble, France) using the ERIXS spectrometer designed jointly by the ESRF and the Politecnico di Milano. G.G. and Y.Y.P. were supported by the by ERC-P-ReXS project (2016-0790) of the Fondazione CARIPLO and Regione Lombardia, in Italy. R.L.G. and T.S. acknowledge support from NSF award DMR-1708334. Computational work was performed on the Sherlock cluster at Stanford University and on resources of the National Energy Research Scientific Computing Center, supported by the US DOE under contract number DE-ACO2-05CH11231.

**Reviewer information** *Nature* thanks D. M. Casa, D. van der Marel and the other anonymous reviewer(s) for their contribution to the peer review of this work.

**Author contributions** W.S.L., G.G., L.B., T.P.D. and Z.X.S. conceived the experiment. M. Hepting, W.S.L., L.C., R.F., Y.Y.P., G.G., M. Hashimoto, K.K. and N.B.B. conducted the experiment at ESRF. M. Hepting, L.C. and W.S.L. analysed the data. E.W.H., W.C.L., B.M. and T.P.D. performed the theoretical calculations. T.S., J.-F.H., C.R.R., Y.S.L. and R.L.G. synthesized and prepared samples for the experiments. M. Hepting, B.M. and W.S.L. wrote the manuscript with input from all authors.

Competing interests The authors declare no competing interests.

## Additional information

**Extended data** is available for this paper at https://doi.org/10.1038/s41586-018-0648-3.

Supplementary information is available for this paper at https://doi.org/10.1038/s41586-018-0648-3.

Reprints and permissions information is available at http://www.nature.com/reprints.

**Correspondence and requests for materials** should be addressed to Z.X.S. or T.P.D. or W.S.L.

**Publisher's note:** Springer Nature remains neutral with regard to jurisdictional claims in published maps and institutional affiliations.

# **METHODS**

The c-axis-oriented LCCO thin films with Ce concentrations of x = 0.11, 0.13, 0.15, 0.17, 0.175 and 0.18 were fabricated on (100) SrTiO<sub>3</sub> substrates by pulsed laser deposition using a KrF excimer laser. The annealing process was optimized for each x. The superconducting  $T_c$  of the x = 0.11 and 0.13 films is around 30 K and around 22 K, respectively. The x = 0.175 and 0.18 films did not show a superconducting transition. The NCCO single crystal with Ce concentration x = 0.15 was grown by the travelling-solvent floating-zone method in O<sub>2</sub> and annealed in Ar at 900 °C for 10 h. The  $T_c$  is about 26 K.

The RIXS measurements were performed at beamline ID32 of the ESRF using the high-resolution 'ERIXS' spectrometer. The scattering angle  $2\theta$  can be changed in a continuous way from 50° to 150°. The samples were mounted on the 6-axis in-vacuum Huber diffractometer/manipulator and cooled to around 20 K. The RIXS data were obtained with incident  $\sigma$  polarization (perpendicular to the scattering plane, high-throughput configuration). The incident photon energy was tuned to the maximum of the Cu  $L_3$  absorption peak at about 931 eV. The energy resolution was  $\Delta E \approx 60$  meV for the x = 0.11, 0.15, 0.17 and 0.18 LCCO sample and  $\Delta E \approx 68$  meV for the x = 0.13 and 0.175 LCCO and the x = 0.15 NCCO sample. The RIXS polarization-resolved measurements were conducted with a wider monochromator exit slit at a resolution of  $\Delta E \approx 85$  meV in order to partly compensate the reduced efficiency of the polarimeter with respect to the normal configuration. For each transferred momentum a non-resonant silver paint or carbon tape spectrum provided the exact position of the elastic (zero energy loss) line. For the polarimetric RIXS measurements of Fig. 1d, e, σ-polarization incident on the sample was used and the graded multilayer served as analyser of the scattered photons, as explained in detail in ref. <sup>33</sup>. We note that Cu L-edge RIXS is the so-called direct RIXS process, involving the resonant transition from the Cu 2p core level to the  $3d_{x^2-y^2}$  orbital, which constitutes the electronic structure near the Fermi energy. The Cu L-edge RIXS is capable of probing a wide range of elementary excitations, including the orbital (that is, the dd-excitations), magnetic excitations, phonons and charged excitations<sup>20</sup>.

In the theory calculations we consider the three-band Hubbard model with the following standard parameters in units of electronvolts:  $U_{\rm dd}=8.5$ ,  $U_{\rm pp}=4.1$ ,  $t_{\rm pd}=1.13$ ,  $t_{\rm pp}=0.49$ ,  $\Delta_{\rm pd}=3.24$  (ref.  $^{34}$ ). Determinant quantum Monte Carlo (DQMC)  $^{35}$  is used to solve the model on a fully periodic  $16\times4$  cluster at a temperature of T=0.125 eV. For each doping, 512 independently seeded Markov chains with 50,000 measurements each are run. The charge susceptibilities obtained by DQMC are analytically continued to real frequency using the maximum entropy method with model functions determined by the first moments of the data  $^{36}$ . The inverse dielectric function plotted in Fig. 3c is obtained via  $\frac{1}{\varepsilon(q,\omega)}=\frac{1}{1+V_q\chi(q,\omega)}$ ,

where  $\chi\left(q,\omega\right)$  is the real frequency charge susceptibility obtained from DQMC and the maximum entropy method. The long-range and 3D Coulomb interactions neglected in the three-band Hubbard model are captured by  $V_q$ . We use the layered electron gas form  $^{37}$ :  $V_q = \frac{d}{2\varepsilon_\infty} \frac{1}{q \left\| \cosh(q \left\| d \right\| - \cos(q_z d) \right\|}$  where d is the interplane spacing

and  $q_{\parallel}$  and  $q_z$  are the in-plane and out-of-plane components of the momentum transfer, respectively.  $\varepsilon_{\infty}$ , the sole free parameter of our calculation, is adjusted to give a roughly 1-eV mode for  $q_z$  = 0 and the smallest non-zero  $q_{\parallel}$  = (0.0625, 0); its value is not varied with doping.

Fit of the plasmon dispersion in the layered electron gas model. We consider the energy—momentum dispersion of a plasmon mode in a layered electron gas model for momentum transfer  $q_{\parallel}$  along the h-direction at fixed out-of-plane momentum transfer values  $q_z$  (along the  $l^*$ -direction). Let d be the spacing between adjacent  ${\rm CuO_2}$  planes and  $q_z d = \pi l^*$  and  $\varepsilon_{\infty}$  be the high-frequency dielectric constant due to the screening by the core electrons. Following ref. <sup>38</sup>, the Coulomb potential of a layered electron gas is:

$$V_q = \alpha^2 \frac{\sinh(q_\parallel d)}{\left[q_\parallel \left[\cosh(q_\parallel d) - \cos(q_z d)\right]\right]}$$

with

$$\alpha = \sqrt{\frac{e^2 d}{2\varepsilon_0 \varepsilon_\infty}}$$

In an isotropic medium it is well-known that the 3D Coulomb potential is  $e^2/\varepsilon_0\varepsilon_\infty q^2$ , while in a 2D plane the Coulomb potential is  $e^2/2\varepsilon_0\varepsilon_\infty q_\parallel$ . These are the two limits of the above form of the layered electron gas, with  $V_q$  becoming  $V_q=e^2/\varepsilon_0\varepsilon_\infty q_\parallel^2$  in the approximation of long wavelengths  $(q_zd<<1$  and  $q_\parallel d<<1$ ), and  $V_q=e^2/2\varepsilon_0\varepsilon_\infty q_\parallel$  for short wavelengths  $(q_\parallel d>>1$ , independent of  $q_z$  momentum).

Here, we use the full form from above and obtain the energy of the plasmon mode by:

$$\omega_{p} \approx q_{\parallel} \sqrt{V_{q}} \approx \alpha \sqrt{\frac{q_{\parallel} \mathrm{sinh}(q_{\parallel} \ d)}{\mathrm{cosh}(q_{\parallel} \ d) - \mathrm{cos}(q_{z} d)}}$$

With this expression we performed least-squares fits of the plasmon energy dispersion, simultaneously for the datasets of  $l^*=0.5$ ,  $l^*=0.825$  and  $l^*=0.9$  with the global fitting parameter  $\alpha$ , yielding  $\alpha=2.06$  (Extended Data Fig. 4). We note that the layered electron gas model does not include strong correlations, which explains the deviations between the experimental data and the model fit.

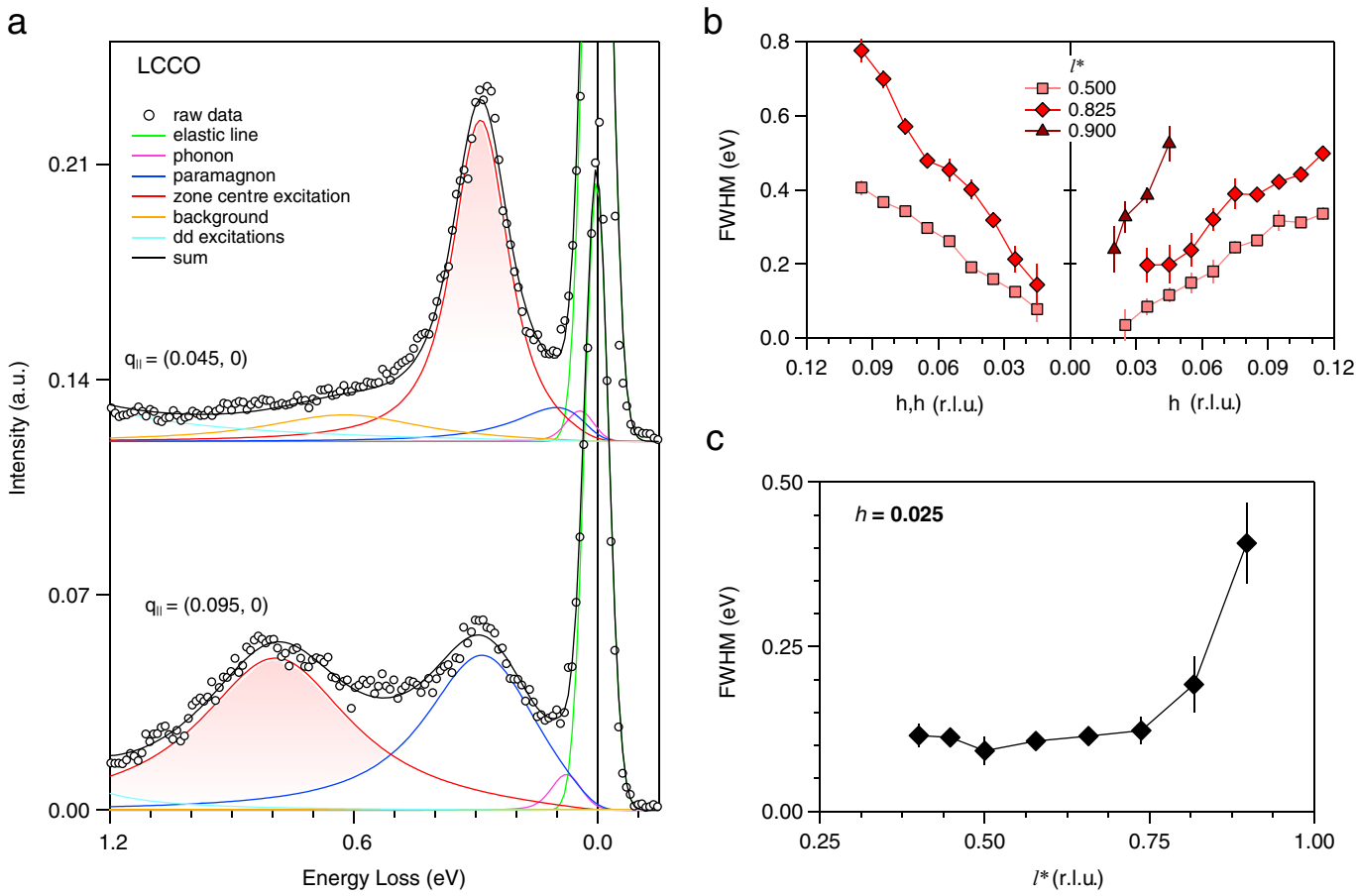
Verifying the systematics of electron doping. To confidently plot the doping dependence shown in Fig. 4, we verified the systematics of electron doping concentration using an internal reference of RIXS spectra—the energy positions of the dd excitations located in the energy range of 1.5–3 eV (Extended Data Fig. 5a). dd excitations are transitions within Cu 3d orbitals; thus, they are forbidden by optical dipole transitions, but allowed in the RIXS process<sup>39</sup>. Because electrondoping primarily fills the Cu  $3d_{x^2-y^2}$  orbital, the energy separation between the Fermi energy  $E_{\rm F}$  and other occupied d-orbitals increases with increasing electron doping. As a consequence, the energy position of the dd excitations—which is essentially the energy separation between  $E_{\rm F}$  and occupied d orbitals—shifts to higher energy loss in the RIXS spectra (Extended Data Fig. 5a and its inset). This shift should correlate with the nominal Ce doping concentration *x*, providing an independent verfication of the electron doping among different samples. Indeed, as shown in Extended Data Fig. 5b, all our samples of x = 0.11, 0.13, 0.15, 0.17 and 0.18 correlate well with x, except for the x = 0.175 sample. This indicates that the actual electron doping concentration of the nominally 'x = 0.175' sample might be affected by some change of oxygen composition or local inhomogeneity. Therefore we did not include the x = 0.175 data in Fig. 4. We emphasize that the qualitative behaviours, that is, the out-of-plane dependence shown in Figs. 1-3, are the same for all doping concentrations of LCCO and also for the NCCO (Extended Data Fig. 3) that were studied in this work.

**Code availability.** Source code for the DQMC simulations is available at https://github.com/cmendl/hubbard-dqmc. Sample input files are included for the three-band Hubbard model studied in this work.

# Data availability

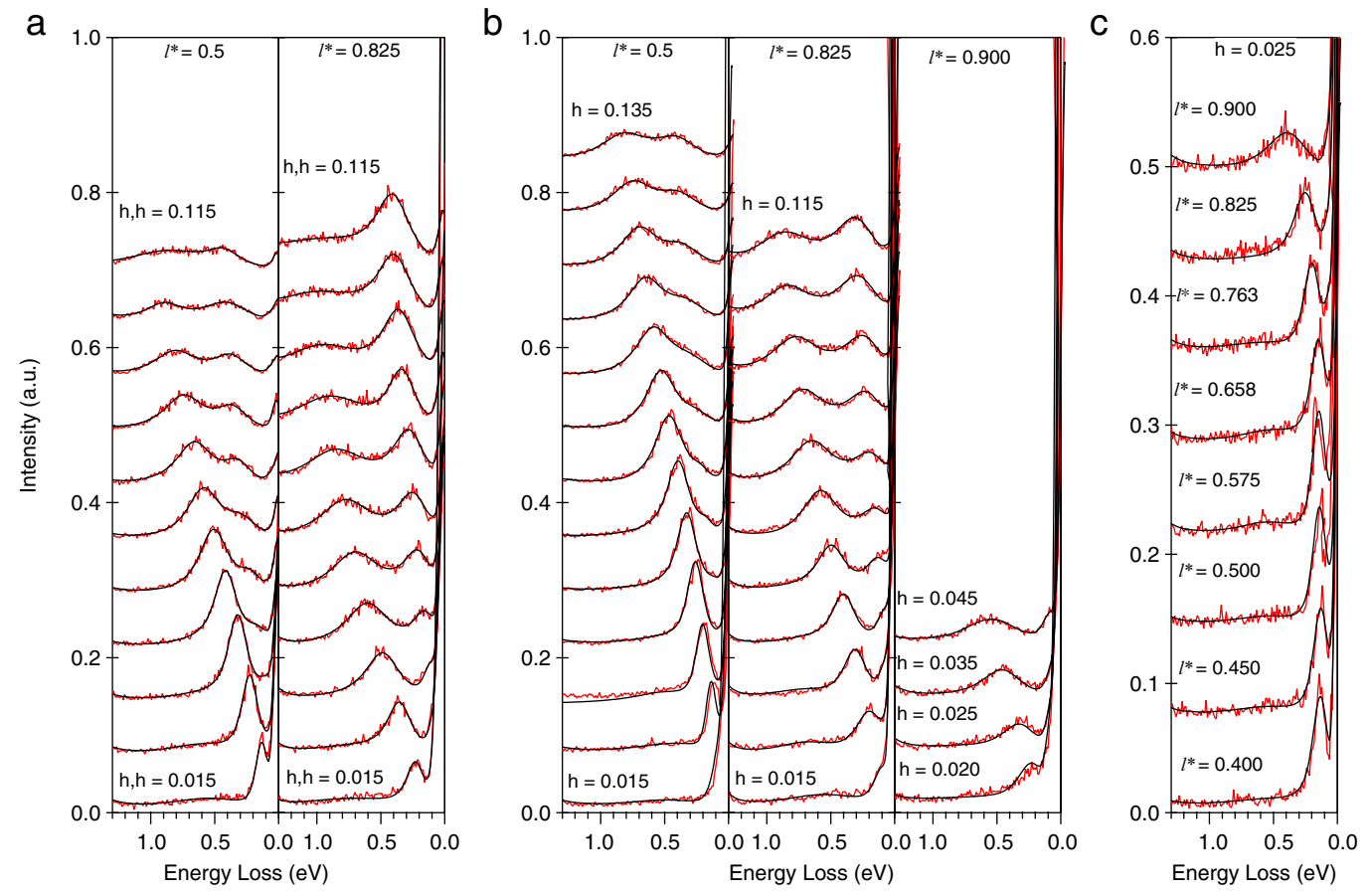
Raw data are included for Figs. 1b-e, 2, 3a, 4, and Extended Data Figs. 1-4. The data that support the plots within this paper and other findings of this study are available from the corresponding authors upon reasonable request.

- Braicovich, L. et al. The simultaneous measurement of energy and linear polarization of the scattered radiation in resonant inelastic soft X-ray scattering Rev. Sci. Instrum. 85, 115104 (2014).
- Kung, Y. F. et al. Characterizing the three-orbital Hubbard model with determinant quantum Monte Carlo. Phys. Rev. B 93, 155166 (2016).
- Blankenbecler, R., Scalapino, D. J. & Sugar, R. L. Monte Carlo calculations of coupled boson-fermion systems. I. Phys. Rev. D 24, 2278 (1981).
- Jarrell, M. & Gubernatis, J. E. Bayesian inference and the analytic continuation of imaginary-time Monte Carlo data. *Phys. Rep.* 269, 133 (1996).
- Fetter, A. L. Electrodynamics of a layered electron gas. I. Single layer. Ann. Phys. 81, 367 (1973).
- Turlakov, M. & Leggett, A. J. Sum rule analysis of umklapp processes and Coulomb energy: application to cuprate superconductivity. *Phys. Rev. B* 67, 094517 (2003)
- Moretti Sala, M. et al. Energy and symmetry of dd excitations in undoped layered cuprates measured by Cu L<sub>3</sub> resonant inelastic X-ray scattering. New J. Phys. 13, 043026 (2011).
- Le Tacon, M. et al. Intense paramagnon excitations in a large family of high-temperature superconductors. Nat. Phys. 7, 725 (2011).



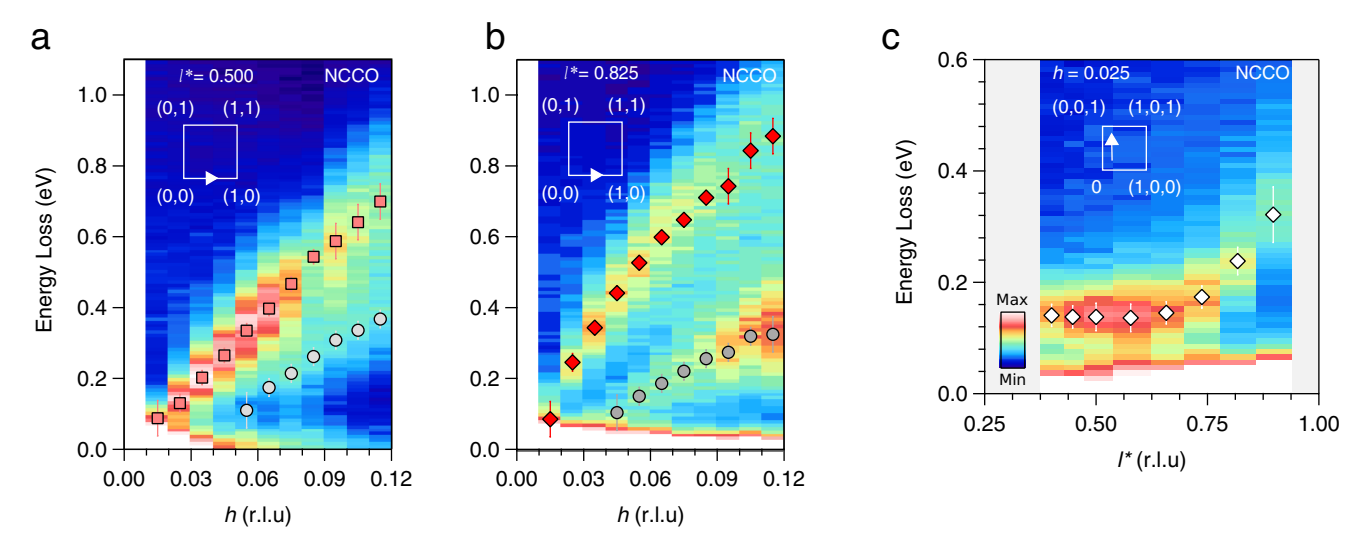
Extended Data Fig. 1 | Fits of the RIXS spectra. a, Fits of LCCO (x=0.175) RIXS spectra at in-plane momentum transfer positions  $q_{\parallel}$ = (0.045 0) and (0.095 0), representative of all fits performed in the scope of this work. The model uses a Gaussian for the elastic peak (green) and anti-symmetrized Lorentzians for all other contributions in the spectrum, convoluted with the energy resolution (here  $\Delta E$  = 68 meV) via Gaussian convolution. The anti-symmetrized Lorentizan is used to ensure zero mode intensity at zero energy loss, as explained in the supplementary information of ref.  $^{40}$ . The peak profiles of the zone centre

excitation (plasmon) are shaded in red. **b**, Full-width at half-maximum (FWHM) of the zone centre excitation (plasmon) as extracted from the fits for momentum transfer along the hh- and h- directions at  $l^*=0.5$ ,  $l^*=0.825$  and  $l^*=0.9$ , corresponding to the fitted peak positions shown in Fig. 2c. Error bars are the standard deviation of the fits. **c**, FWHM of the zone centre excitation (plasmon) as extracted from the fits for momentum transfer along the out-of-plane direction at h=0.025. The panel corresponds to the fitted peak positions shown in Fig. 3a.



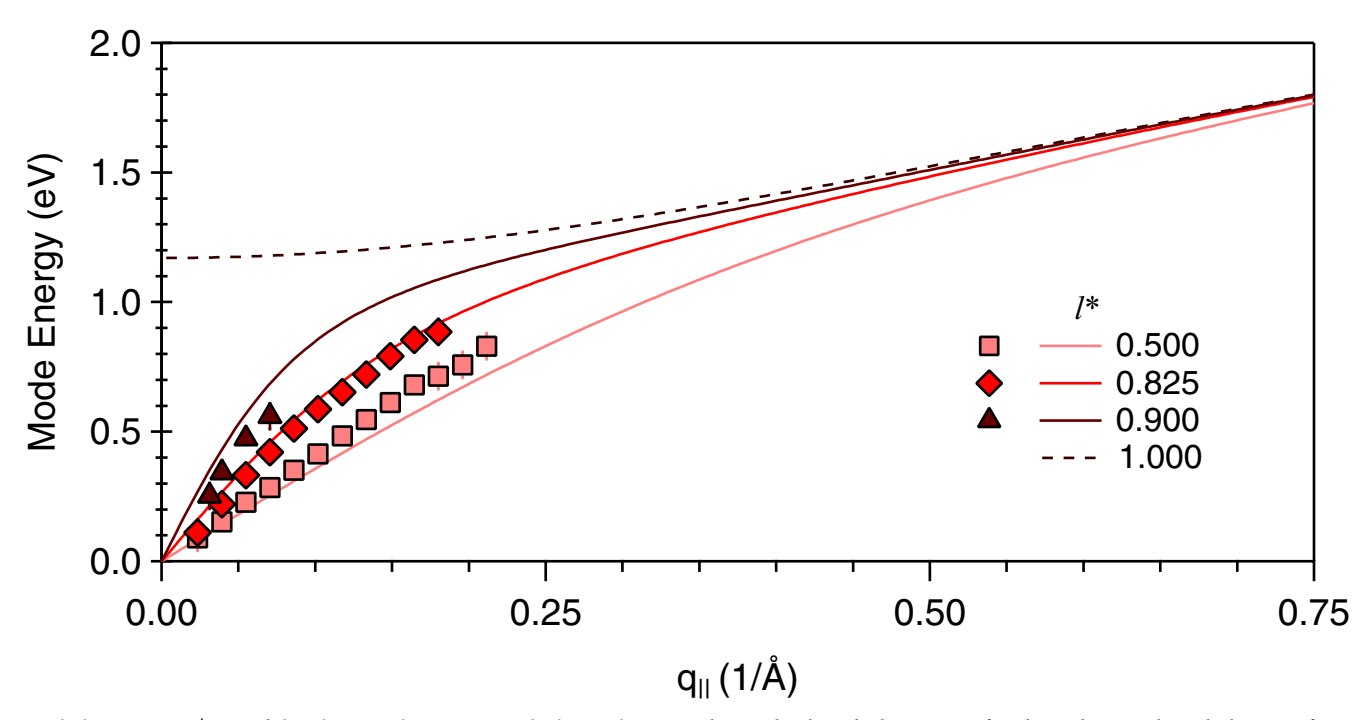
**Extended Data Fig. 2** | **Raw data and fits of the RIXS spectra. a, b,** Raw RIXS spectra (red) of LCCO (x = 0.175) together with the fits (solid black lines) for momentum transfer along the hh-direction (**a**) and h-direction (**b**)

at different  $l^*$ . The spectra are offset in the vertical direction for clarity. c, Raw RIXS spectra together with the fits for momentum transfer along the  $l^*$ -direction at h=0.025.



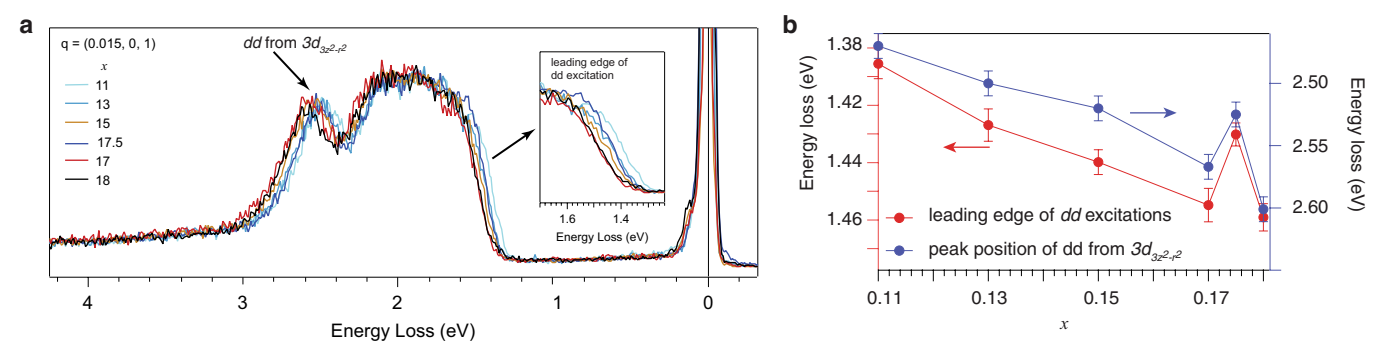
**Extended Data Fig. 3** | Three-dimensionality of the zone centre excitations in NCCO. a, b, RIXS intensity maps of NCCO (x=0.15) for momentum transfer along the h-direction at l\*=0.5 and l\*=0.825. Red and grey symbols indicate least-squares-fit peak positions of the zone centre excitation and the paramagnon, respectively. The inset indicates the probe direction in reciprocal space. c, RIXS intensity map of NCCO

(x = 0.15) for momentum transfer along the out-of-plane direction at h = 0.025. White symbols indicate fitted peak positions of the zone centre excitation. Error bars are estimated from the uncertainty in energy-loss reference-point determination ( $\pm$ 0.01 eV) together with the standard deviation of the fits.



Extended Data Fig. 4 | Fits of the plasmon dispersion in the layered electron gas model. a, Fits (solid lines) of the mode energies of LCCO (x=0.175) (red symbols) as a function of in-plane momentum transfer  $q_{\parallel}$  along the h-direction at  $l^*=0.5$ ,  $l^*=0.825$  and  $l^*=0.9$ . The fit is global,

that is, the three  $l^*$  datasets are fitted simultaneously with the same fit parameter, as described in the Methods. Error bars of the data points are the same as those estimated in Fig. 2c.



Extended Data Fig. 5 | Verification of electron doping systematics via dd excitations in the RIXS spectra. a, dd excitations in RIXS spectra at momentum transfer (0.015, 0, 1) taken from samples with different Ce doping concentrations x. The energy positions of dd excitations shift to higher energy with increasing electron doping, which can be used as an internal reference to verify the doping concentrations. The inset shows a zoom-in of the leading-edge region of the dd excitations. b, The correlation

between the Ce concentration x and the energy of the dd-leading edge (inflection point) and the  $3d_{z^2-r^2}$  peak. All samples show good correlation except for the x=0.175 sample, indicating a larger uncertainty of its doping concentration. Thus, the x=0.175 data were not included in Fig. 4. The error bars are estimated from the standard deviation of the fit used to determine the energy of the dd-leading edge and the  $3d_{z^2-r^2}$  peak.